Enhancing Uniform Crystallization and Grain Growth of Halide Perovskite Films by Combining Multi-Pass Inkjet Printing and Antisolvent Bathing

Marc Migliozzi†, Vishal Pal†, Joseph Damian, Youngsoo Jung, Jung-Kun Lee*

Department of Mechanical Engineering and Material Science, University of Pittsburgh, Pittsburgh, PA 15261, USA

Abstract

Recent manufacturing of perovskite solar cells (PSC) is moving beyond a spin coating technique. Among several new methods of the large-area PSCs, inkjet printing has emerged as a promising alternative to spin coating due to the high degree of control on printed film area and low material waste. In the inkjet printing of PSCs, one important question is how to remove redundant excess solvent and facilitate the crystallization of the perovskite phase. Along with inkjet printing, we employ an antisolvent bathing. This work reports how the inkjet printing parameters and antisolvent bathing compositions affect the microstructure and initial efficiency of inkjet-printed PSCs. The halide perovskite films are submerged in the antisolvent of different temperatures to observe the formation of an intermediate phase and the evolution of perovskite phase. By observing the phase evolution using XRD, an optimized antisolvent bath duration was achieved for DE condition. We also report an enhanced PCE and larger grain size with two sequential passes of inkjet deposited perovskite, and propose the dissolution of homogeneous nucleation sites as a mechanism for larger grains. Finally, with multi pass inkjet printing and cold antisolvent DE bathing, a champion device with 15.02% PCE was achieved.

Keywords: perovskite solar cells, inkjet printing, antisolvent bathing

†: Equal contribution, *: Corresponding author: jul37@pitt.edu

1. Introduction

Hybrid organic-inorganic perovskite solar cells (PSCs) present a promising path towards lower cost solar energy when compared to conventional silicon-based technology. PSCs made of $CH_3NH_3PbI_3$ were first reported in 2009 by Kojima et. al. with a power conversion efficiency (PCE) of 3.8% [1-4]. Since then, the field has rapidly developed, and recent PCEs as high as 26.7% in 2024 have been reported [5]. These high PCEs are possible due to perovskites' defect tolerance and high light absorption, which contribute to the conversion of most incident photons to electricity without internal loss. [1,2]

Spin coating of a perovskite precursor solution followed by antisolvent dripping or nitrogen quenching is the most widely used method for PSC fabrication at laboratory scale. However, spin coating is not a scalable method, as it cannot uniformly deposit large areas and also produces significant material waste. To replace the spin coating, many research groups have turned to methods such as slot-die casting [3-4,6-7], blade coating [8–10], and inkjet printing (IJP) [11–22]. Among these candidates, IJP is unique in that it allows for precise control over the deposited active area, which reduces perovskite waste and potentially negates the need for extra material removal steps such as laser scribing for module fabrication. In inkjet printing, a piezoelectric printhead deposits a precursor ink, followed by the removal of the solvents and crystallization of the perovskite film. Two-step printing of the perovskite film is also reported. In this method, two reagent inks are printed sequentially, which potentially allows for a higher degree of control over the perovskite crystallization. [21]

The inkjet printing of perovskite films requires the simultaneous development of piezoelectric waveform parameters (voltage, rise/fall/dwell time) and ink concentration. Additionally, parameters such as printhead orifice diameter or precursor temperature can affect the printability of an ink. Solutions that are too viscous may not eject uniformly from the printhead, while low concentration solutions may produce droplets that do not stay together upon ejection from the printhead (satellites droplets). The inkjet printing community often uses two dimensionless parameters, Ohnesorge (Oh) and Reynolds (Re) number, to quantify printability of a solution, as shown in equations (1-2). The Oh number considers solution rheology and printhead width. In the following equation for Oh, η is viscosity, ρ is density, σ is surface tension, and d is the width of the printhead.

$$Oh = \frac{\eta}{\sqrt{\rho \cdot \sigma \cdot d}} \quad (1)$$

$$Re = \frac{\rho \cdot v \cdot d}{\eta} \quad (2)$$

Equation (2) on the Re number includes the velocity of the droplet which is obtained using the printer's integrated camera. As shown in Fig. 1, these two parameters are often plotted against each other. This helps to find an optimum solution of printability which is experimentally verified (Fig. S1). When the perovskite solution is printed, it is essential to develop an ink that fits within these constraints while also meeting final film thickness requirements.

A scientifically meaningful factor to the understanding of the crystallization in the IJP of the perovskite film is the precipitation and dissolution of nucleation sites prior to thermal annealing. Mathies *et al*. reported a slight increase (145 nm to 170 nm) in grain size with increasing sublayers of precursor solution, which they credit to the redissolving of seed crystals in preceding layers during the ink-jet printing [16]. A similar effect was found in a spray coating-based experiment. The redissolving of the crystallized film can merge small grains to make a new film made up of larger grains [23]. An increase in grain size is generally seen as advantageous in terms of optoelectronic properties, as grain boundaries can act as carrier trap states, which cause non-radiative recombination [24].

Most IJP studies of PSCs have relied on vacuum flashing (or vacuum quenching) for solvent extraction and intermediate phase formation [25]. In this process, a vacuum chamber is used to rapidly remove solvents. In this work we examined a method called "antisolvent bathing" that is compatible with a general wet chemical process of the perovskite solar cells and does not require isolating the films to a high vacuum level. The application of an "antisolvent" bathing has been used to rapidly remove solvents from a wet film and induce an intermediate phase. The "bathing" refers to the process of submerging the as-deposited perovskite films in an antisolvent after deposition. In a solvent bath, the antisolvent washes away precursor solvent in the film through diffusion but it does not dissolve the perovskite solutes. In contrast to antisolvent dripping as a part of the spin coating step, the antisolvent bathing is simple and compatible to a role-to-role process which is suitable for the manufacturing of large-scale PSCs [26-27].

The implications of applying antisolvent using the bathing method are not well studied, especially in the context of as-deposited IJP films. A few groups have successfully applied the antisolvent bathing approach in the fabrication of halide perovskite films. Moon *et al.* optimized the miscibility and temperature of the antisolvent to control the nucleation kinetics and microstructure of the film by using a binary antisolvent mixture [26]. Suppressed homogeneous nucleation by reducing the miscibility and temperature of the antisolvent promotes heterogeneous nucleation at the electron transport-perovskite interface and leads to large, vertically oriented grains [26-27]. Seo *et al.* found that a binary mixture of low-toxicity tert-butyl alcohol (t-BA) and ethyl acetate (EA) successfully converted the precursor film to the uniform $FAPbI_3$ film [28]. We try to reproduce this result with our $MAPbI_3$ films. Similarly, Tu *et al.* added formamidinium chloride (FACl) to 2-pentanol to facilitate the antisolvent precipitation and enhance the crystalline quality of triple cation halide perovskite film [29].

This study reports the printing process of the perovskite precursor solution using a single nozzle printer, the antisolvent bathing, and the following crystallization process of the IJPed perovskite films. Concerning antisolvent bathing, we systematically studied the effect of the polarity difference between the solvent and the antisolvent on the crystallization and grain growth of the film. In addition, two antisolvent bath temperatures (0 and 21 ± 2 °C) were chosen to find a relation between antisolvent bath temperature and film morphology and PCE. It is found that the antisolvent's polarity, miscibility, and coordination with precursor solution solvents and solutes all affect diffusion rates of solvent out of the wet film, as well as crystallization kinetics and final film morphology. The miscibility of two solvents and the precipitation of nuclei can be related to a difference in their polarities. In general, polar solvent dissolves in polar solvent and vice versa. Therefore, the microstructure of the film produced by the antisolvent bathing highly depends on the nature of antisolvent such as the polarity. Notably, a large difference in polarity between an

antisolvent, such as diethyl ether (0.117) and a coordinating solvent, such as DMSO (0.444), allows for an intermediate phase (sometimes expressed as PbI_2·DMSO) to form [30,31], as DMSO is not completely removed from the film prior to annealing.

2 Experimental Methods

2.1 Materials

Methylammonium iodide (MAI 99.9%) was purchased from Ossila, TiO_2 paste (mesoporous-TiO_2) (SC-HT040) was purchased from SHARECHEM, Lead Iodide (PbI_2 99.99%), dimethyl sulfoxide (DMSO, anhydrous, ≥99.9%), dimethylformamide (DMF, anhydrous, 99.8%), Ti-diisopropoxide (97%), acetonitrile (anhydrous, 99.8%), chlorobenzene (anhydrous, 99.8%), 2,2′,7,7′-tetrakis(N,N-dip-methoxyphenylamino)-9,9′-spirobifluorene (spiro-OMeTAD), bis-(trifluoromethane) sulfonimide lithium salt (Li-TFSI, 99.95%), 4-*tert*-butylpyridin (TBP, 96%) were purchased from Sigma Aldrich, diethyl ether(anhydrous, 99.5%), anisole(99.0%), ethyl acetate(99.9%), t-butyl acetate(99%) were purchased from Fischer scientific. Fluorine-doped tin oxide (FTO) coated glass substrates were purchased from MSE Supplies LLC. All chemicals were used without any further modifications.

2.2 Device Fabrication

Fluorine doped tin oxide (FTO) coated glass substrates were cut into 2×2 cm^2 and ultrasonic cleaned for 15 minutes each in acetone, deionized water, and ethanol. The substrates were dried followed by UV-ozone treatment for 15 minutes. A blocking-TiO_2 solution prepared by mixing 0.971ml Ti-diisopropoxide in 4ml 1-butanol was spin coated in ambient on the FTO substrates at 3000 rpm for 30 seconds. Next, the substrates were annealed at 150 °C for 15 minutes. A mesoporous-TiO_2 solution was prepared by dissolving TiO_2 paste in ethanol (1:5.5 weight ratio). The mesoporous-TiO_2 solution was spin coated over the blocking-TiO_2 layer at 4000 rpm for 30 seconds. After both ETL layers were deposited, substrates were annealed in a furnace at 500°C for 1 hour.

Perovskite precursor solution was prepared by dissolving MAI (1M) and PbI_2 (1M) in DMSO:DMF (78ul of DMSO and 507ul of DMF, 2:13 in a volume ratio) solvent. The solution was stirred overnight. For the deposition of the perovskite film, substrates were first treated in a UV-Ozone cleaner for 5 minutes. Next, a single-nozzle inkjet printer (JetLab 4, MicroFab) with the PH-41 printhead assembly (60 μm printhead diameter) was used to deposit the perovskite film in an ambient environment (room temperature) with a relative humidity of 25 ± 10 %. Solution vials were opened and exposed to ambient conditions immediately before filling the printhead reservoir, and solutions were filtered through a PTFE 0.45 μm filter to prevent printhead clogging. Two primary scripts were used for inkjet printing: 1-pass (single pass) and 2-pass (multi-pass). In a single pass inkjet printing method, all ink was dropped in a single pass of the printer head over a $1cm^2$ area. Single pass printing took 45 seconds and dropped 4200 droplets in $1cm^2$ area. In the multi-pass method, the print head finished its first step, then went back to the origin and ran again. The droplet density was 4950 droplets/cm^2 for multi-pass printing. We added a slightly larger volume of the ink during the multi pass printing because it allowed more time for drying of the

printed ink. The initial pass dropped roughly two-thirds of the total ink, and a second pass dropped the remaining one third of the ink. The total time of printing for a 1 cm^2 active area by the multi-pass method was 90 seconds. We optimized the drop spacing in x and y direction (d_x, d_y) where $d_y = 1.67d_x$ for both single pass and multi-pass. The optimized piezoelectric printhead parameters for stable precursor droplets are as follows: Voltage of 36 V, a rise/fall time of 4 μs, a dwell time of 25 μs, and a back pressure of -3.4 psi.

Printed substrates were immediately submerged into an antisolvent bath filled with diethyl ether (DE), anisole (AN), ethyl acetate (EA), or a mixture of tert-butyl alcohol (t-BA) and EA (t-BA:EA = 7:3 in volume) until the films turned light brown. For the cold antisolvent conditions, the solvents were stored in a refrigerator prior to use, then the crystallizing dish containing the antisolvent was put on ice during use. This was followed by annealing at 100 ºC for 10 minutes on a hot plate in ambient. A video showing the process is available in Supporting Information. Next, the hole transport layer (spiro-OMeTAD) was deposited via spin coating in ambient with a spin rate of 4000 rpm for 30 seconds. This solution was prepared by dissolving (36 mg of spiro-OMeTAD in 500 uL chlorobenzene) 8.8 μL of a Li-TFSI solution (360 mg of Li-TFSI in 500 uL of acetonitrile), and (14.4 μL of TBP) together. Finally, Au contacts (80 nm) were deposited using an electron-beam evaporator (MEB550S, Plassys).

2.3 Device Characterization

Microstructure of the IJPed films was observed using a scanning electron microscope (SEM, Apreo, FEI). Crystal structure studies were carried out using X-Ray diffraction (XRD, D8 discover, Bruker). A Cu Kα radiation (λ = 1.5406 Å) was used as a radiation source. Photovoltaic properties of the solar cell device were measured by an electrochemical workstation (CHI660D, CHI) under an AM 1.5G solar simulator (XES-301S, SAN-EI). A 0.14 cm^2 aperture mask was used for measurements. After Au top electrode was deposited by evaporation, the performance of solar cells was measured immediately without light soaking (i.e. exposure to light for a certain period before J-V sweeps). Forward bias scans were run from 1.2 to -0.1 V for reverse scans, and -0.1 to 1.2 V for forward scans. The scan rate was run at 0.1 V/s, with a sensitivity of 0.001 A/V.

3. Results

3.1 Inkjet printing of the perovskite film

In preliminary research, we found an effective approach to achieving the uniform film formation of adequate thickness was to first tune the precursor ink concentration, and then optimize inkjet piezoelectric parameters for stable droplet formation. We tested perovskite precursor concentrations from 1.43 to 2.0 M to find inks that could reliably produce droplets from a 60 μm diameter printhead. We found Oh and Re numbers for each ink, labeled I1-I5 in order of increasing concentration, and plotted them to screen for printability (Fig. 1). Three solutions (I3-I5) fell within the printability window. As expected, satellite droplets were often observed when the solution I1 was printed. I3 solution (the concentration of 1.7 M) enabled the consistent printing of the uniform film without satellite droplets. I5 solution (the concentration of 2 M) resulted in visibly nonuniform films, due to lack of spreading and coalescence (Fig. 1).

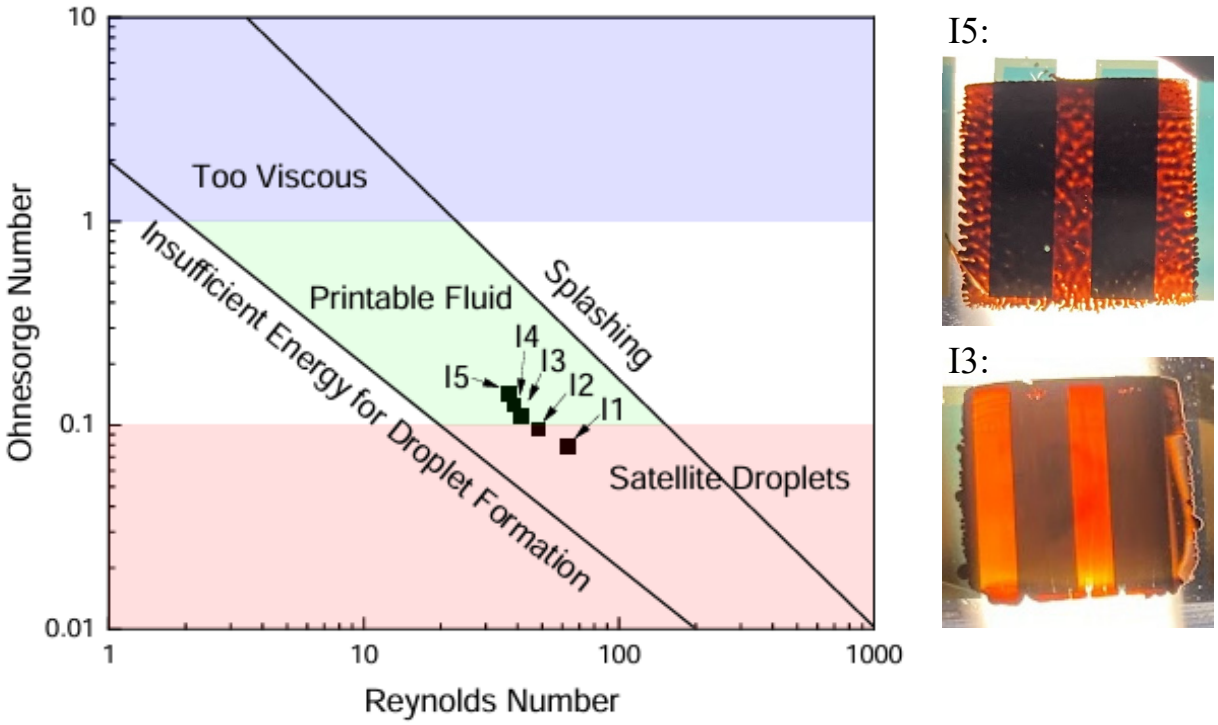

Figure 1. (Left) the Oh. vs. Re printability plot [32] showing the effect of the solution concentration on the morphology of printed films - five concentrations of the perovskite precursor ink in this study are labeled I1-I5, where I5 and I1 is the most and least concentrated solution, respectively; (right) photos of two films made from I5 (top) and I3 (bottom) - the highly concentrated ink (I5) does not form a uniform film due to increased viscosity and reduced flow over the substrate, though it falls in a printable range of the Oh. vs. Re printability plot.

In addition, spacing between droplets was found to be the primary factor in how the solution flowed over the substrate after deposition. For printing 1 cm^2 active areas, we observed a net flow of the deposited solution along the printhead moving direction when the drop spacing was equal in both dimensions (Fig. S1). For better printing, the drop spacing was increased in the direction of flow, and proportionally decreased in the direction perpendicular to flow so that the overall dispensed volume remained constant. Our optimized droplet spacing was 0.12 × 0.20 mm, or approximately 1.67× larger in the direction of flow. We deposited 4200 droplets cm^{-2} to attain a thickness of 500 nm. Higher droplet densities resulted in more uncontrolled flow across the substrate.

Two more parameters, namely ink concentration and number of printing pass were also optimized. Optimizing these parameters involves studying the microstructure of fully annealed perovskite film. However, to grow a film with good microstructure we needed to optimize the antisolvent bathing process first. A study on choosing the best antisolvent and time of antisolvent bathing is presented in section 3.2. After diethyl ether was chosen as the best antisolvent. the following printing parameters were optimized.

While optimizing ink concentration, we simultaneously developed a solvent ratio that allowed for a longer processing window, as it took our printer 90 seconds to deposit a 1 cm^2 active area. We also examined the morphology of annealed films to see how ratios of DMSO to DMF (1:4, 2:13, 1:8 in volume) affected film formation. The 1:4 ratio of DMSO:DMF is a commonly used benchmark for spin coating. However, IJP films made from 1:4 DMSO:DMF were visibly hazy after annealing and contained many pinholes, as shown in Fig. S2. This hazy structure was attributed to excess coordinating DMSO in the film. In the inkjet printing, there is no additional force repelling the DMSO from the deposited film such as centrifugal force of the spinning process. This indicates that the precursor solution of the inkjet printing needs to contain less DMSO than that of the spin-coating. On the other hand, films made of 1:8 DMSO:DMF did not cover one edge of the substrate (Fig. S2). The high volatility of DMF caused fast drying in the films around one edge, which resulted in the low nucleation density and uncontrolled crystal growth. The 2:13 solvent volume ratio balanced the issues pertaining to excess residual DMSO and fast DMF evaporation. These films gave us a longer processing window than the 1:4 DMSO:DMF films, and the lower volume of residual DMSO compared to 1:8 DMSO:DMF films allowed for dense and pinhole free films. We note that the 2:13 solvent ratio was nearly a 1:1 molar ratio of PbI_2:DMSO, which is important for the complete formation of an intermediate phase.

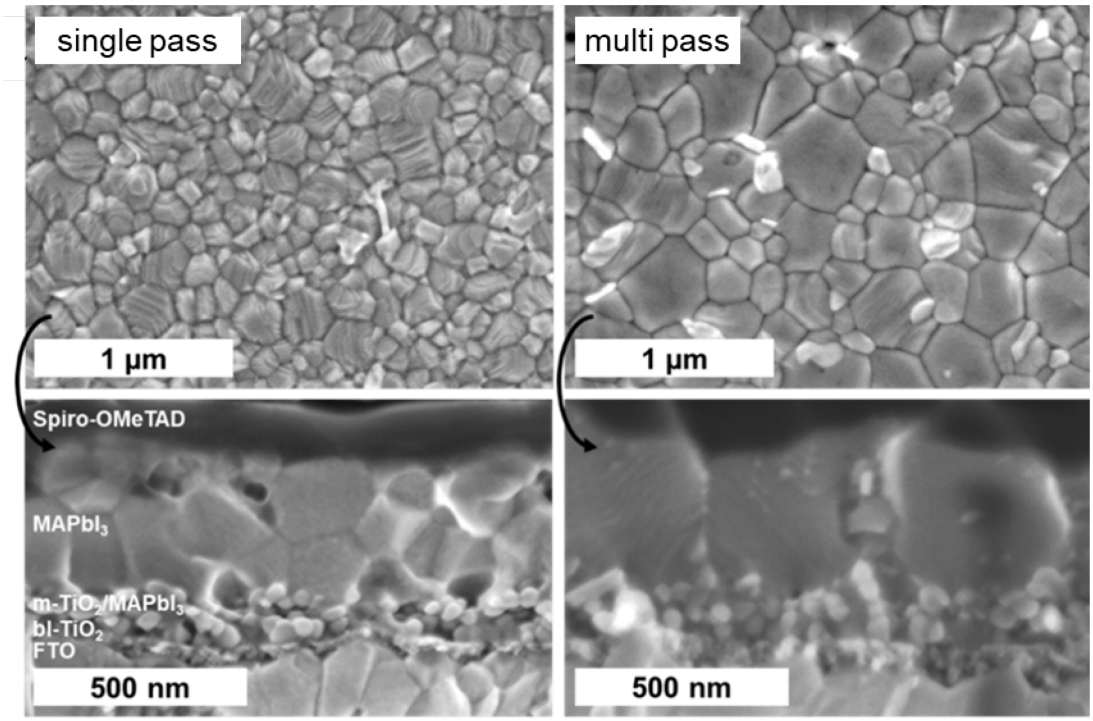

Figure 2. Plan-view and cross-section scanning electron micrographs of single pass (left) and multi pass (right) printed films made from room temperature diethyl ether antisolvent bathing.

Our last printing parameter of interest was the effect of a number of printhead passes. The printhead passes each printing point of the substrate one time or two times in the single pass or multiple pass printing. One and two pass scripts were generated to drop 4200 drops/cm^2 and 4950 drops/cm^2 for single pass and multi pass, respectively. The process was optimized where the initial pass dropped roughly two-thirds of the ink, and a second pass dropped the remaining third. If the first pass dropped half of the ink, evaporation of the thin film was too rapid, and we could not form

a cohesive perovskite base layer. SEM micrographs shown in Fig. 2 suggested that our multi-pass method resulted in larger perovskite grains. In cross-sectional micrographs, the multi-pass films exhibit significantly less horizontal grain boundaries, with respect to the transport layers, than the single-pass films.

These observations suggest that in the case of multi-pass films, the second pass of ink redissolves homogeneous nucleation sites near the top surface of film while keeping heterogeneous sites near the perovskite-TiO_2 interface intact as opposed to single pass films where nucleation likely starts near the surface of the film. The lower concentration of homogeneous nucleation sites before antisolvent bathing results in larger grains due to fewer overall nucleation sites. If solvent of the printed film dries for a longer period, another second phase (PbI_2) appears that can act as a homogeneous nucleation sites. This is the case of a single pass printing. In the second pass printing, this precipitated PbI_2 is redissolved and the homogeneous nucleation is suppressed. The reference here shows the relation between PbI_2 crystallites and $MAPbI_3$ films. The study reports that (001) plane of PbI_2 plates is converted to (202) plane of $MAPbI_3$ plates. This information is added in the revised manuscript with references [33,34]. In the case of single-pass films, which take about 45 seconds to print 1×1 cm^2 film, homogeneous nucleation is prevalent as DMF evaporation lowers the concentration of the film and grains become smaller.

3.2 Antisolvent bathing for highly crystalline films

Immediately after printing, the film was submerged in an antisolvent bath. Four initial antisolvents of different polarities were chosen for the bathing process: diethyl ether (DE) (relative polarity = 0.117), anisole (AN) (relative polarity = 0.198), ethyl acetate (EA) (relative polarity = 0.228), and the binary antisolvent system of tert-butyl alcohol (t-BA) (relative polarity = 0.389) dissolved EA (t-BA:EA 7:3 vol., relative polarity = 0.340). The relative polarity of DMF is 0.386. The film was kept in the antisolvent bath until the color of the printed film changed from yellow to brown, as shown in Fig. 3. This color change is the indication of nucleation initiation in the film [28]. A mixture of t-BA/EA with relative polarity 0.340, took the least time to show color change, followed by EA (relative polarity = 0.228), then anisole (relative polarity = 0.198). Of the antisolvents tested, DE with the lowest relative polarity of 0.117 showed the slowest conversion to an intermediate phase. This indicates that a difference in the polarity of antisolvent and DMF is an important parameter in the antisolvent crystallization.

An antisolvent with high relative polarity easily dissolves the DMF (0.386) and creates an antisolvent-DMF mixture. Additionally, if the solubility of an organosulfur compound (DMSO) (0.444) in the antisolvent-DMF mixture is high, then it prevents the formation of an intermediate adduct, PbI_2·DMSO. This lack of the intermediate phase results in the direct conversion of PbI_2 and MAI to the perovskite phase ($MAPbI_3$). In that case, the unreacted PbI_2 can precipitate first and acts as seed crystal with plate-like morphology. On the other hand, when the polarity difference becomes large due to use of weakly polar or non-polar antisolvent such as DE, the antisolvent-DMF mixture solution inside the printed layer has a low solubility for not only precursor materials, but also DMSO. The reduction in solubility allows the precursor to form an intermediate phase ($MAPbI_3$·DMSO adducts). The formation of such intermediate adducts, and subsequent nucleation leads to formation of a uniform and dense perovskite layer.

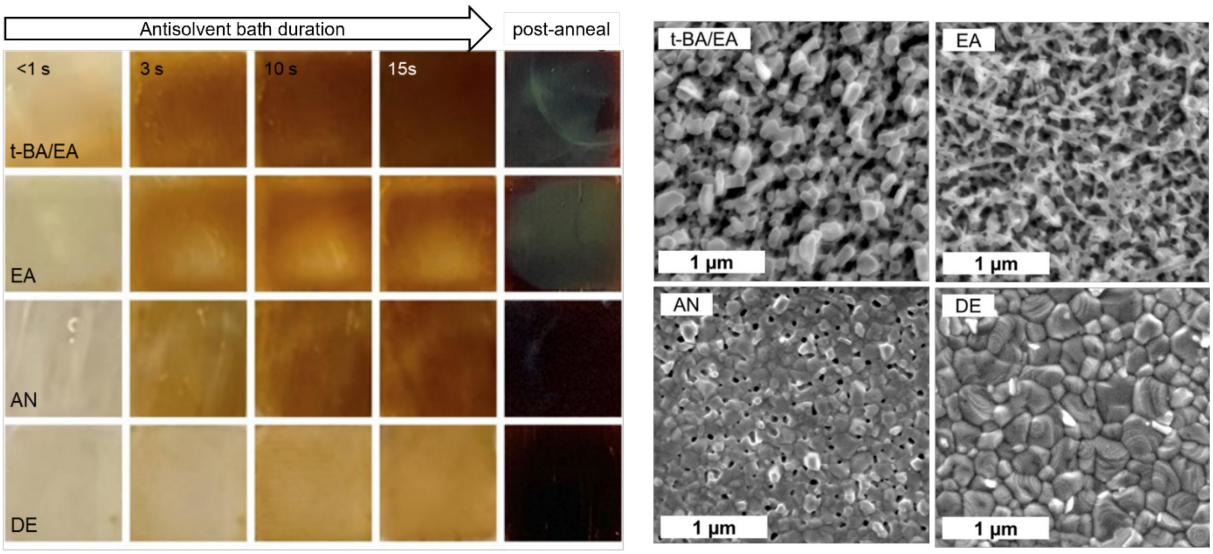

Figure 3. (left) Photos for evolution of perovskite nucleation while submerged in different antisolvents. The rightmost column shows films post anneal. (right) plan-view SEM micrographs of post anneal inkjet-printed films prepared in different antisolvent bath compositions.

As seen in Fig. 3, films that were washed in DE show the highly uniform microstructure with dense and compact grains. This can be explained by the relatively low polarity of DE as compared to all other antisolvents used in this study. When the precursor perovskite film was washed with the antisolvent of moderate polarity such as anisole, the resulting microstructure shows small grains with many pinholes, as seen in Fig. 3. The relatively higher polarity of anisole as compared to DE increases the miscibility of the antisolvent with DMSO. In this case, annealed films have grains of irregular shapes and defects such as pinholes. The films washed with EA and t-BA/EA are made up of large, plate and needle-like grains as shown in Fig. 3. We attribute this morphology to the lack of intermediate phase caused by washing of DMSO from the film during the antisolvent bathing step.

Fig. 4a shows XRD of the inkjet-printed films that were bathed in our four antisolvent baths. The films were not heat-treated after the antisolvent bathing to preserve the intermediate phase if formed. Samples were dipped in each antisolvent for three seconds. When DE was used as antisolvent, the XRD pattern shows not only the perovskite phase, but also the intermediate phase (PbI_2·DMSO). However, the anisole-treated film shows mainly the peaks of the perovskite phase with weak traces of the intermediate phase. When EA and t-BA/EA were used as antisolvent, only perovskite peaks were found and no intermediate phase peaks were observed. This suggests that the fast color change of the printed films by the antisolvent of the high polarity is due to the rapid transformation to the perovskite phase and the antisolvent of the low polarity promotes the formation of the intermediate phase during the antisolvent bathing.
To confirm the formation of the intermediate phase and understand its evolution with respect to time of dipping in the DE bath, we varied the bathing time from 3 seconds to 30 seconds. 5 samples were prepared with the bathing time of 3, 5, 10, 15, and 30 seconds. No annealing was done on these films to preserve the intermediate phases. XRD analysis on these samples show the appearance of the intermediate phase for short bathing and the pure perovskite phase for long

bathing. For samples with three seconds of bathing in DE bath, Fig. 4b shows a dominant characteristic peak of an intermediate phase at 2θ of 6.7°, 7.4° and 9.4°. These peaks can be indexed as planes (002), (021), and (022) peaks of the intermediate phase [35,36]. The intensity of intermediate phase peaks reduced as the time was increased to 5 seconds, indicating the conversion of the intermediate phase to the perovskite phase in the antisolvent bath. This is also consistent with the color change observed in DE washed films at five seconds and later. Washing for longer durations resulted in formation of pure perovskite phase. After ten seconds of antisolvent submersion, no intermediate phase peaks were observed.

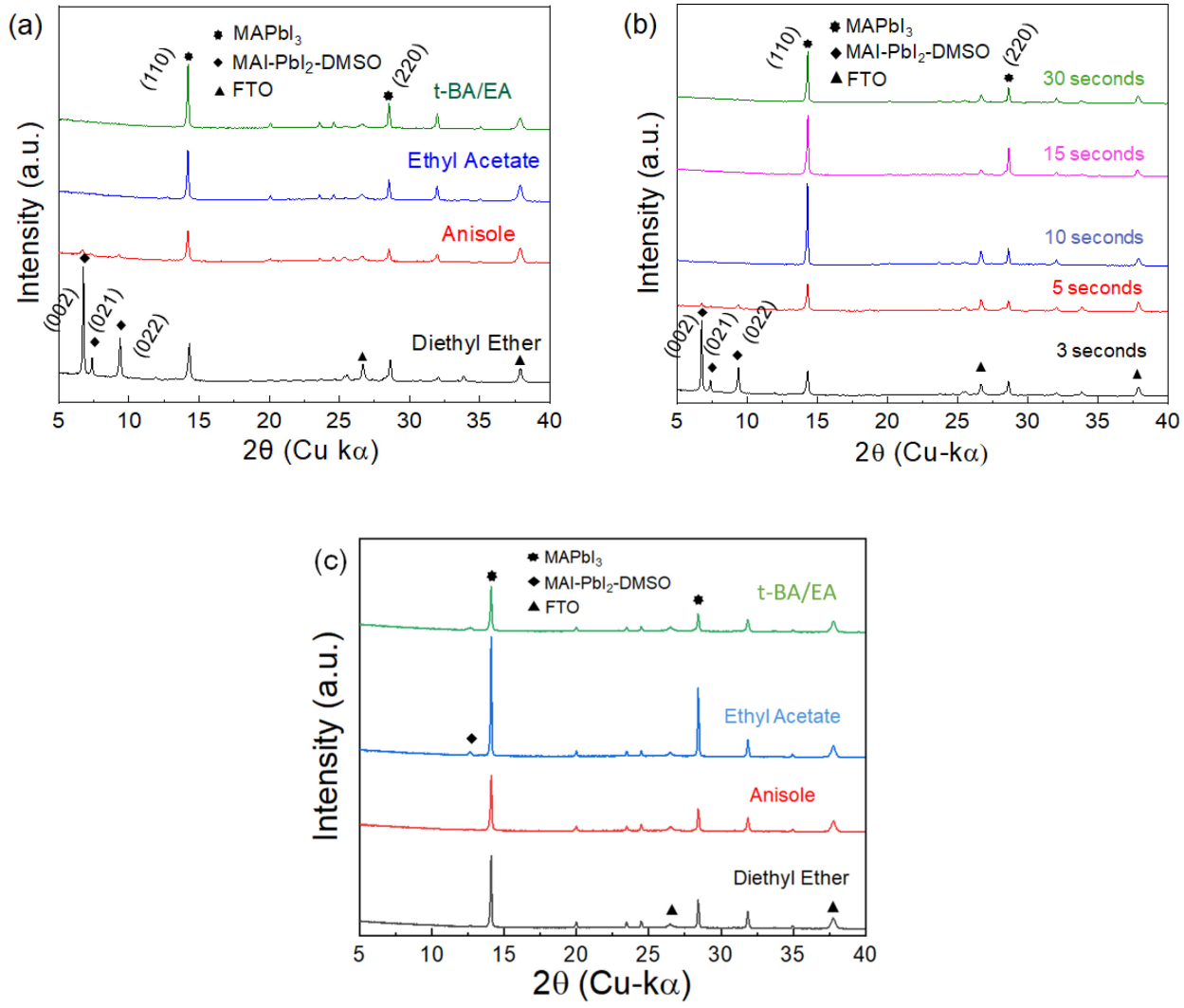

Figure 4. a) X-ray diffraction pattern for 3 seconds wash in different antisolvents, **b)** X-ray diffraction pattern of intermediate phase (MAI-PbI_2-DMSO) formed without annealing step by varying the bathing time in DE, **c)** X-ray diffraction pattern of inkjet-printed films (single pass) after the antisolvent bathing and thermal annealing at 100 °C.

Fig. 4c shows the XRD patterns of the films which were treated by antisolvents and then thermally annealed. A faint PbI_2 peak was observed at $2\theta=12.66°$ for EA and t-BA/EA bathed samples, signifying incomplete conversion. This peak corresponds to unconverted or excess PbI_2. Fully crystallized perovskite phase peaks were observed for samples washed with anisole and DE. No PbI_2 peak is observed in films washed in diethyl ether or anisole, indicating complete reaction of MAI and PbI_2.

Based on these observations, we propose two primary requirements for antisolvent bathing IJP perovskite films. First, the antisolvent should have low polarity. The polarity difference between antisolvent and solvents should be large enough to prevent any removal of a coordinating solvent such as DMSO, but still remove DMF from the wet film. Larger polarity difference also provides a longer window for the intermediate phase formation. Additionally, the films should be taken out of the bath within five seconds of dipping to induce the formation of intermediate phase but prevent its conversion to final perovskite film.

3.3 Effect of antisolvent bath temperature on crystallization and performance of solar cells

The role of antisolvent during antisolvent bathing is to extract the solvent from the inkjet deposited film and enter the solution to form an antisolvent-solvent mixture. The solubility for the precursor materials becomes low in the solvent-antisolvent mixture. This, in turn, allows the film to reach a supersaturation state where the nucleation can take place. Therefore, the rate of solvent extraction and solvent-antisolvent mixing in the film controls not only the rate of supersaturation but also controls the crystallization kinetics and eventually nucleation and growth. In this study, it is found that the temperature of the antisolvent bath has a considerable effect on the solvent extraction and mixing rate.

We used our DE antisolvent bath to study the effect of bathing temperature on film crystallization. Two conditions were tested: room temperature ($21 \pm 2°C$) and cold ($1 \pm 2°C$). As seen in fig. 5, the films turn brown at a slower rate in the cold antisolvent bath, which implies that the lower temperature slows down the diffusion of solvents at an atomic level and reduces the solvent extraction rate. We believe reduced temperature primarily affect the diffusion rate of solvents, not the nucleation since the nucleation occurs after the sample is taken out of bath as shown in XRD previously. The reduced solvents extraction provides a larger window for intermediate phase formation which leads to a final well crystallized perovskite film with improved grain growth.

SEM cross-sectional images, also seen in Fig. 5, revealed a drastic difference in films washed in room temperature baths compared to cold baths. Films washed in room temperature baths were made up of small grains (200 ± 100 nm) with horizontal grain boundaries in the bulk of the film. Films in the cold antisolvent bath showed larger grains. Fig. 5 shows cold antisolvent bathing with multi-pass films, which has the largest grains on average (500 nm). These films also had the largest distribution of grain size, with some grains measuring over a micron, while others were just over 200 nm.

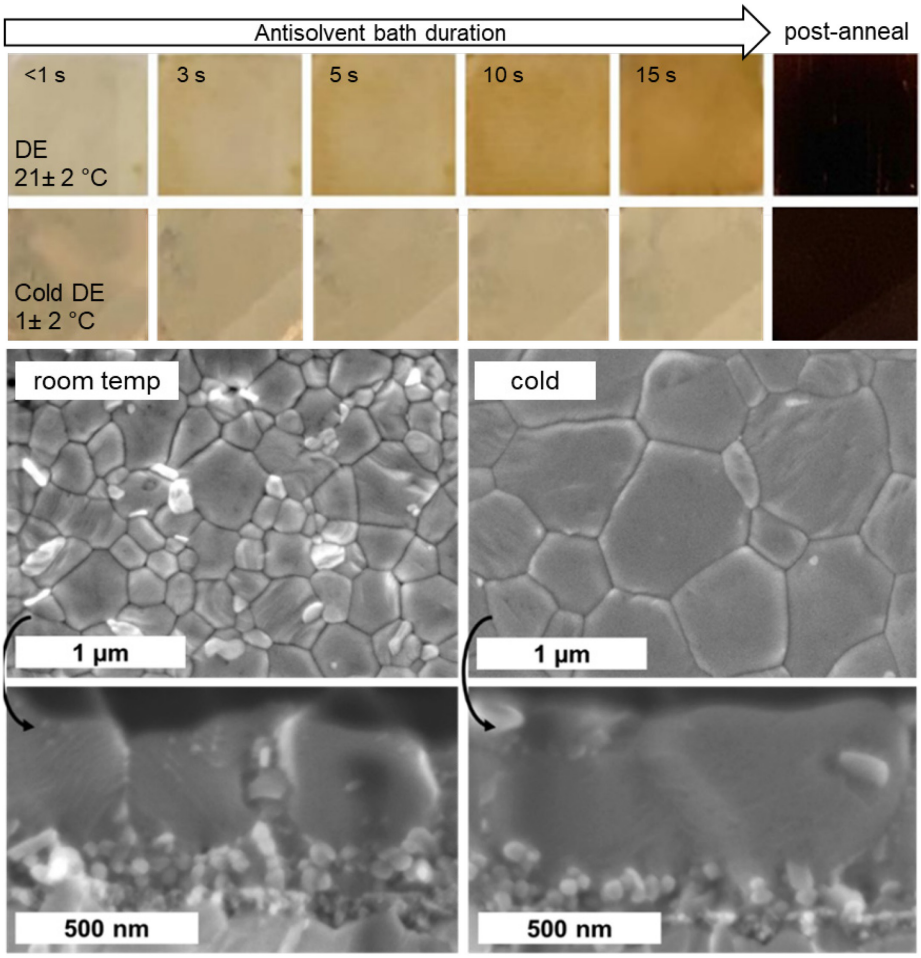

Figure 5. (top) Change in the inkjet-printed films as a function of submerging time in room-temperature or cold DE baths – the post-anneal film is also added as a reference. (bottom) plan-view and cross-section SEM images of room temperature and cold bathed films.

Further XRD analysis was carried out for room temperature washed and cold washed films to compare their crystallinity, as seen in Fig. 6. Dominant characteristic peaks of $MAPbI_3$ at 2θ of 14.1°, 28.5°, and 31.7° were observed in both films. These peaks can be assigned to (110), (220) and (310) planes for 14.1°, 28.5°, and 31.7°, respectively. To compare the grain orientation, we use the XRD peak intensity ratio of (110)/(310) planes and (220)/(310) planes. The peak intensity ratio values for room temperature washed samples were calculated to be 5.09 and 1.97 for I_{110}/I_{310} and I_{220}/I_{310} respectively. The intensity ratio values increased to 9.12 and 3.05 for I_{110}/I_{310} and I_{220}/I_{310} respectively in case of cold washed samples. The higher intensity ratio for cold washed samples suggests higher preferred orientation of grains along (110) plane in this case.

Fig. 6a shows J-V curves for the champion room temperature washed and cold washed PSCs. These solar cell performance parameters for champion devices and average over five devices are shown in Table 1. For room temperature antisolvent washing, the champion device shows a PCE of 13.98%, with open circuit voltage (V_{oc}) of 1.017V, short circuit current density (J_{sc}) of 19.30 mA/cm^2 and fill factor (FF) of 71.21%. An average PCE of 13.12% was obtained for the 5 best devices. Average PCE value increased to 14.38% when a cold antisolvent washing was used with

the champion device shows a PCE of 15.02%, open circuit voltage (V_{oc}) of 1.019V, short circuit current density (J_{sc}) of 21.59 mA/cm^2 and fill factor (FF) of 68.26%.

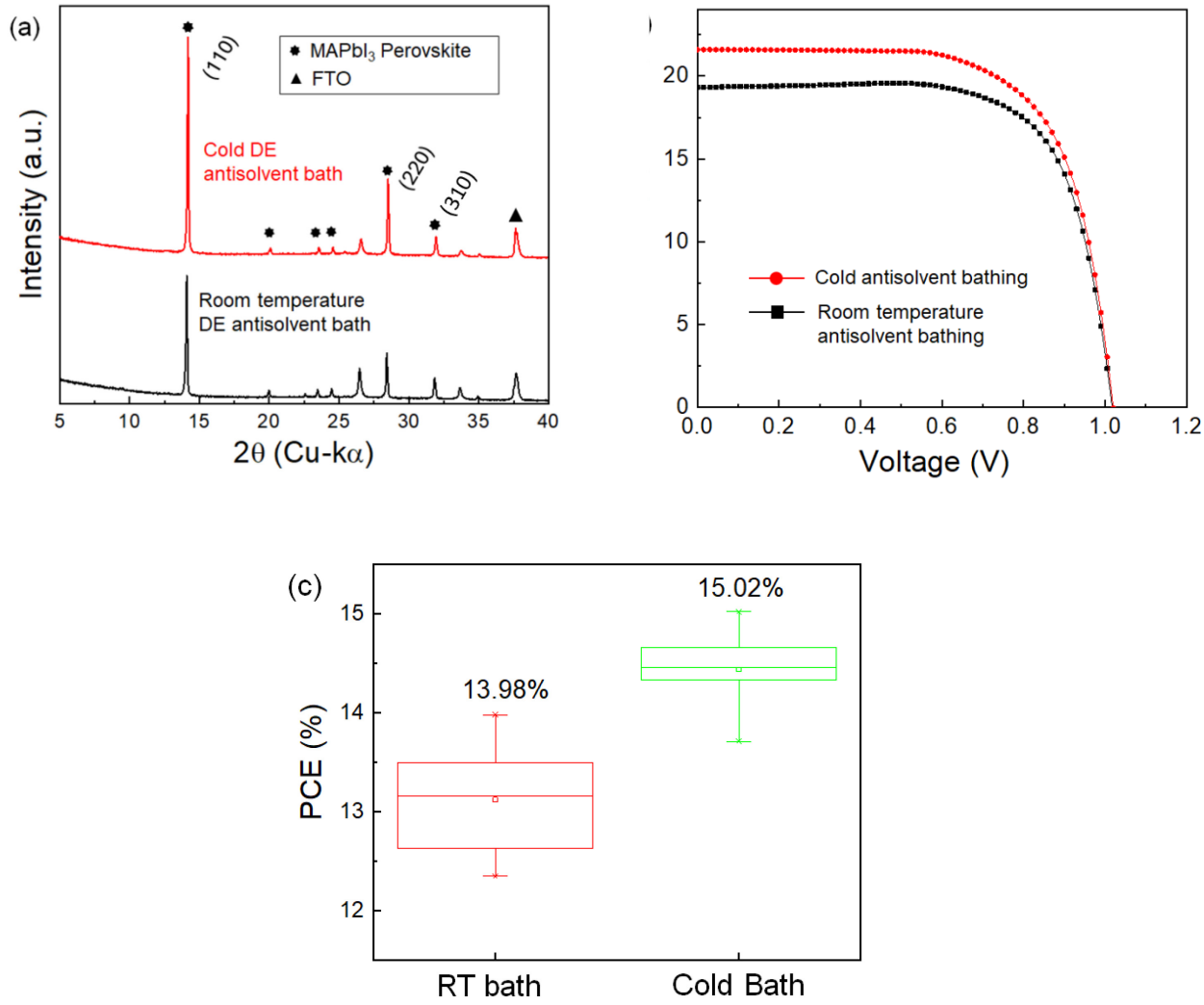

Figure 6. a) X-ray diffraction pattern of $MAPbI_3$ layer after room temperature bath and cold bath in DE, **b)** J-V curves of a champion solar cell of $MAPbI_3$ film from room temperature and cold antisolvent bathing. **c)** PCE statistics box chart for room temperature and cold antisolvent bath.

This suggests that homogeneous nucleation sites were able to propagate during the bathing step. The cold antisolvent-bathed films are made up of large, vertically aligned orientations. It is likely that the lower energy cold antisolvent system suppressed homogeneous nucleation site formation, which is consistent with the fact that homogeneous nucleation sites have a higher free energy barrier than heterogeneous sites. Since DE has low boiling point, it evaporates quickly as the sample is taken out of bath. Fast evaporation of DE can lead to uneven crystallization. Low temperature of bath prevents rapid evaporation of antisolvent after taking out of bath. Maintaining the supersaturated state for a longer time. If the bath temperature decreases, the DE evaporation

slows down allowing more time for film growth which result in better film quality and large grains. Large perovskite grains with reduced grain boundaries allow better charge extraction resulting in higher J_{sc}.

Table 1. Comparison of room temperature washed, and cold washed device performance parameters obtained from J-V curve.

Device Type	J_{SC} (mA/cm^2)	V_{OC} (V)	Efficiency (%)	Fill Factor
Cold bath - best	21.59	1.019	15.02	68.26
Cold bath - average	20.22 ± 1.18	1.019 ± 0.001	14.38 ± 0.46	69.89 ± 2.50
Room temp - best	19.30	1.017	13.98	71.21
Room temp - average	19.07 ± 0.35	1.006 ± 0.008	13.12 ± 0.58	68.31 ± 1.84

Conclusion

In this work, we successfully prepared PSCs by combining the inkjet printing and antisolvent bathing and demonstrated the effect of the polarity of the antisolvent on the microstructure of halide perovskite films. A 2:13 DMSO:DMF volume ratio (or near 1:1 molar DMSO:PbI_2 ratio) in a 1.7 M ink is stable for inkjet printing and compatible with antisolvent bathing. The difference in polarity of solvents and antisolvents proved to be a valuable indicator of if an intermediate phase would form, which in our case was essential for dense grain growth. We also showed that multi-pass printing and cold bathing can enhance grain size. Cold antisolvent bathing in particular showed preferred orientation of grain along the (110) plane which improved the device performance. These results show how final film morphology, even in a relatively defect tolerant material, can have an impact on device performance. With our optimized multi pass inkjet printing and cold DE antisolvent bathing method, we obtained a champion PCE of 15.02%.

Acknowledgements

This work was supported by National Science Foundation (NSF-2130804, NSF 2314036) and Korea Institute of Energy Technology Evaluation and Planning grant funded by the Korea government (202113091010010).

References

1. C. Wehrenfennig, GE. Eperon, MB. Johnston, HJ. Snaith, LM. Herz, *Adv Mater.* **2014** *26(10)*:1584-9.

2. T. Chen, W. Chen, B.J. Foley, J. Lee, J.P.C. Ruff, J.Y. Peter Ko, C.M. Brown, L.W. Harriger, D. Zhang, C. Park, M. Yoon, Y. Chang, J.J. Choi, S.H. Lee, *Proc. Natl. Acad. Sci. U.S.A.* **2017** 114 (29) 7519-7524

3. R. Patidar, D. Burkitt, K. Hooper, D. Richards, T. Watson, *MTC* **2020**, *22*, 100808.

4. Y.-C. Huang, C.-F. Li, Z.-H. Huang, P.-H. Liu, C.-S. Tsao, *Solar Energy* **2019,** *177*, 255.

5. Best Research-Cell Efficiency Chart | Photovoltaic Research | NREL (Revision 09-23-2024).

6. J. Li, J. Dagar, O. Shargaieva, M. A. Flatken, H. Köbler, M. Fenske, C. Schultz, B. Stegemann, J. Just, D. M. Többens, A. Abate, R. Munir, E. Unger, *Adv. Energy Mater.* **2021**, *11*, 2003460.

7. D.S. Ham, W.J. Choi, H. Yun, M. Kim, D.-H. Yeo, S. Lee, B.J. Kim, J.H.Lee, *ACS Appl. Energy Mater.* **2021** *4* (8), 7611.

8. J. Li, R. Munir, Y. Fan, T. Niu, Y. Liu, Y. Zhong, Z. Yang, Y. Tian, B. Liu, J. Sun, D.-M. Smilgies, S. Thoroddsen, A. Amassian, K. Zhao, S. Liu, *Joule* **2018**, *2*, 1313.

9. C. Li, J. Yin, R. Chen, X. Lv, X. Feng, Y. Wu, J. Cao *J Am Chem Soc* **2019,** *141* (15), 6345.

10. S. Razza, F.D. Giacomo, F. Matteocci, L. Cinà, A.L. Palma, S. Casaluci, P. Cameron, A. D'Epifanio, S. Licoccia, A. Reale, T.M. Brown, A.D. Carlo, *J. Power Sources* **2015**, *277*, 286

11. F. Mathies, H. Eggers, B.S. Richards, G. Hernandez-Sosa, U. Lemmer, U.W. Paetzold, *ACS Appl. Energy Mater.* **2018,** *1* (5), 1834.

12. H. Eggers, F. Schackmar, T. Abzieher, Q. Sun, U. Lemmer, Y. Vaynzof, B. S. Richards, G. Hernandez-Sosa, U. W. Paetzold, *Adv. Energy Mater.* **2020**, *10*, 1903184.

13. A. Karavioti, D.A. Chalkias, G. Katsagounos, A. Mourtzikou, A.N. Kalarakis, E. Stathatos, *Electronics* **2021**, *10*, 1904.

14. L. Zhang, S. Chen, X. Wang, D. Wang, Y. Li, Q. Ai, X. Sun, J. Chen, Y. Li, X. Jiang, S. Yang, B. Xu, *Sol. RRL*, **2021**, *5*, 2100106.

15. Z. Li, P. Li, G. Chen, Y. Cheng, X. Pi, X. Yu, D. Yang, L. Han, Y. Zhang, Y. Song, *ACS Appl. Mater. Interfaces.* **2020** *12* (35), 39082.

16. F. Mathies, T. Abzieher, A. Hochstuhl, K. Glaser, A. Colsmann, U.W. Paetzold, G. Hernandez-Sosa, U. Lemmer, A. Quintilla, *J. Mater. Chem. A* **2016**,*4*, 19207-19213.

17. A. Verma, D. Martineau, S. Abdolhosseinzadeh, J. Heier, F. Nüesch, *Mater. Adv.* **2020**, *1*, 153-160

18. F. Schackmar, H. Eggers, M. Frericks, B. S. Richards, U. Lemmer, G. Hernandez-Sosa, U. W. Paetzold, *Adv. Mater. Technol.* **2021**, *6*, 2000271.

19. A. Giuri, E. Saleh, A. Listorti, S. Colella, A. Rizzo, C. Tuck, C.C. Esposito, *Nanomaterials (Basel)* **2019**, *9*(4), 582

20. C. Liang, P. Li, H. Gu, Y. Zhang, F. Li, Y. Song, G. Shao, N. Mathews, G. Xing, *Sol. RRL*, **2018**, *2*, 1700217.

21. P. Li, C. Liang, B. Bao, Y. Li, X. Hu, Y. Wang, Y. Zhang, F. Li, G. Shao, Y. Song, *Nano Energy* **2018***, 46*, 203.

22. Z. Wei, H. Chen, K. Yan, S. Yang, *Angew. Chem. Int. Ed.* **2014**, *53*, 13239.

23. J.H. Heo, M.H. Lee, M.H. Jang, S.H. Im, *J. Mater. Chem. A* **2016**, *4*, 17636.

24. X. Xu, Y. Sun, D. He, Z. Liang, G. Liu, S. Xu, Z. Li, L. Zhu, X. Pan*, J. Mater. Chem. C* **2021**, *9*, 208.

25. F. Schackmar, H. Eggers, M. Frericks, B. S. Richards, U. Lemmer, G. Hernandez-Sosa, U. W. Paetzold, *Adv. Mater. Technol.* **2021**, *6*, 2000271

26. G. Jang, S. Ma, H.-C. Kwon, S. Goh, H. Ban, J. Lee, C.U. Lee, J. Moon, *Chem. Eng. J.* **2021***, 423*, 130078.

27. G. Jang, H.-C. Kwon, S. Ma, S.-C. Yun, H. Yang, J. Moon, *Adv. Energy Mater.* **2019**, *9*, 1901719.

28. Y.Y. Kim, T.Y. Yang, R. Suhonen, A. Kemppainen, K. Hwang, N.J. Jeon, J. Seo, *Nat Commun.* **2020**, *11*, 5146.

29. Y. Zhang, Y. Tu, X. Yang, R. Su, W. Yang, M. Yu, Y. Wang, W. Huang, Q. Gong, R. Zhu, *ACS Appl. Mater. Interfaces.* **2020,** *12* (22), 24905.

30. Y. Bai, S. Xiao, C. Hu, T. Zhang, X. Meng, Q. Li, Y. Yang, K.S. Wong, H. Chen, S. Yang, Nano Energy, **2017**, *34*, 58.

31. Y. Yao, X. Zou, J. Cheng, D. Chen, C. Chang, T. Ling, H. Ren, *Crystals* **2019**, *9*, 151.

32. G. H. McKinley and M. Renardy, "Wolfgang von Ohnesorge," Physics of Fluids, vol. 23, no. 12, **2011**.

33. T.M. Brenner, Y. Rakita, Y. Orr, E. Klein, I. Feldman, M. Elbaum, D. Cahen, G. Hodes, *Chem. Mater.* **2016**, *28* (18), 6501.

34. Z. Song, S.C. Watthage, A.B. Phillips, B.L. Tompkins, R. J. Ellingson, M.J. Heben, *Chem. Mater.* **2015**, *27*(13), 4612.

35. N.J. Jeon, J.H. Noh, Y.C. Kim, W.S. Yang, S. Ryu, S.I. Seok, *Nature Mater.* **2014**, *13*, 897. 36. S. Chen, X. Xiao, B. Chen, L.L. Kelly, J. Zhao, Y. Lin, M.F. Toney, J. Huang, Sci. Adv. **2021**, *7*, eabb2412.

Supporting Information

Enhancing Uniform Crystallization and Grain Growth of Halide Perovskite Films by Combining Multi-Pass Inkjet Printing and Antisolvent Bathing

Marc Migliozzi[†], Vishal Pal[†], Joseph Damian, Youngsoo Jung, Jung-Kun Lee*

Department of Mechanical Engineering and Material Science, University of Pittsburgh, Pittsburgh, PA 15261, USA

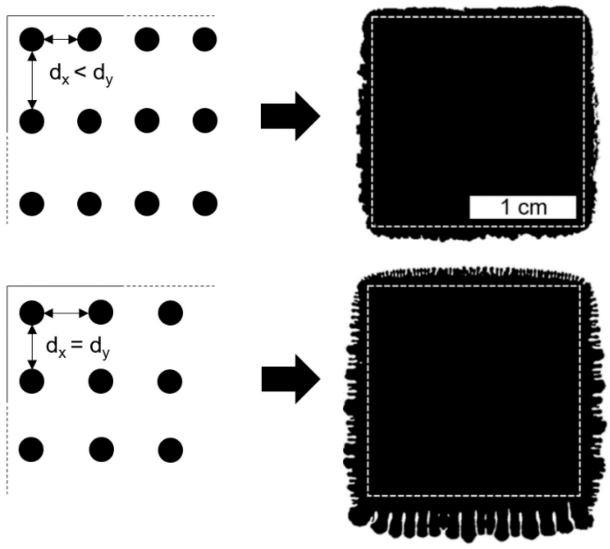

Figure S1. Effect of drop spacing on spreading of solution. Print pattern (left) and monochrome images (right) of evenly distributed flow when $d_y=1.67d_x$ and uncontrolled flow when $d_y=d_x$

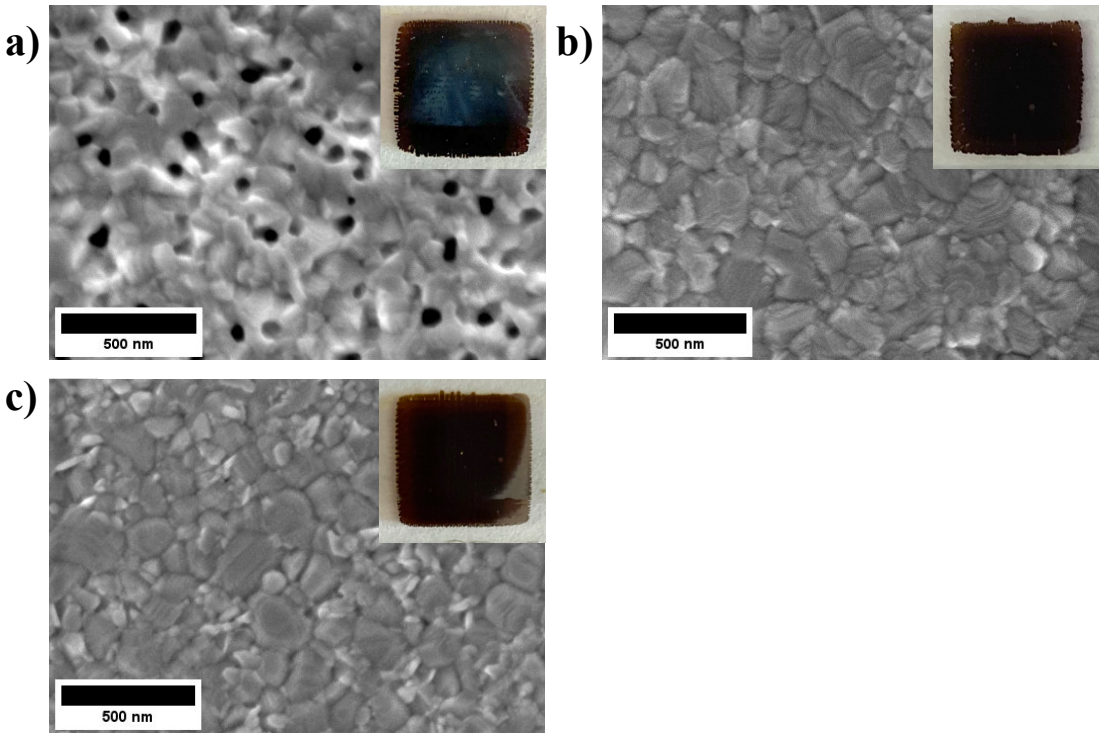

Figure S2. Effect of DMSO:DMF vol. solvent ratio on film morphology. **a** 1:4 DMSO:DMF films have many pinholes and the film is hazy. **b** 2:13 DMSO:DMF films have dense polycrystalline structure with no pinholes. Film is reflective and has no hazy regions. **c** 1:8 DMSO:DMF films show similar structure to 2:13 films, but the increased vol% of volatile DMF leads to evaporation of film on edges.

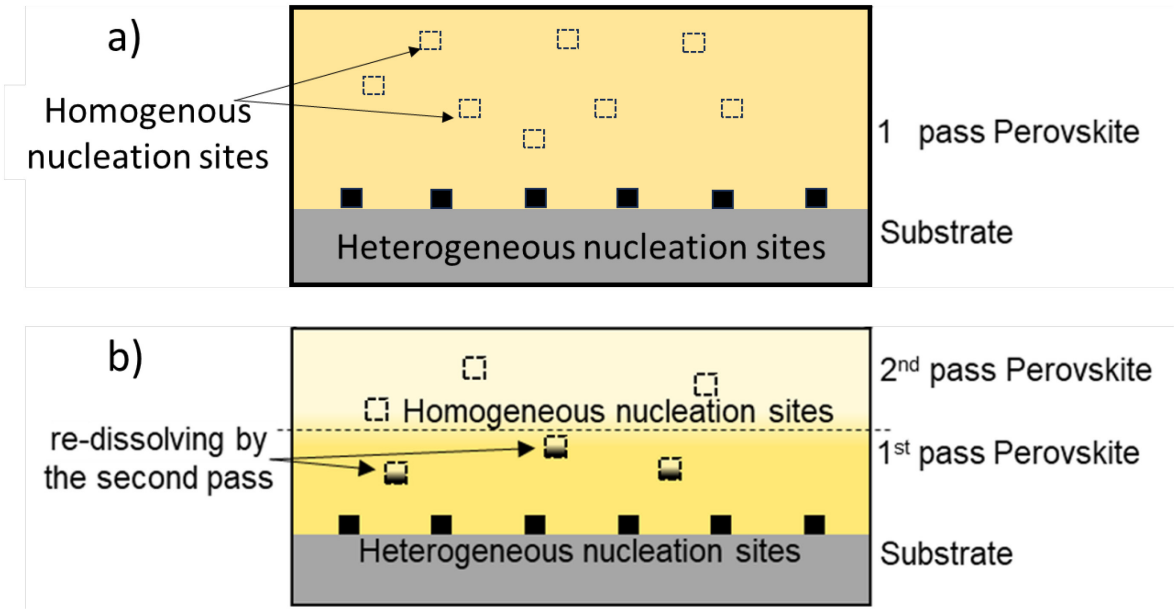

Figure S3. A potential schematic of homogenous and heterogenous nucleation sites in a) single-pass and b) multi-pass inkjet printed films.

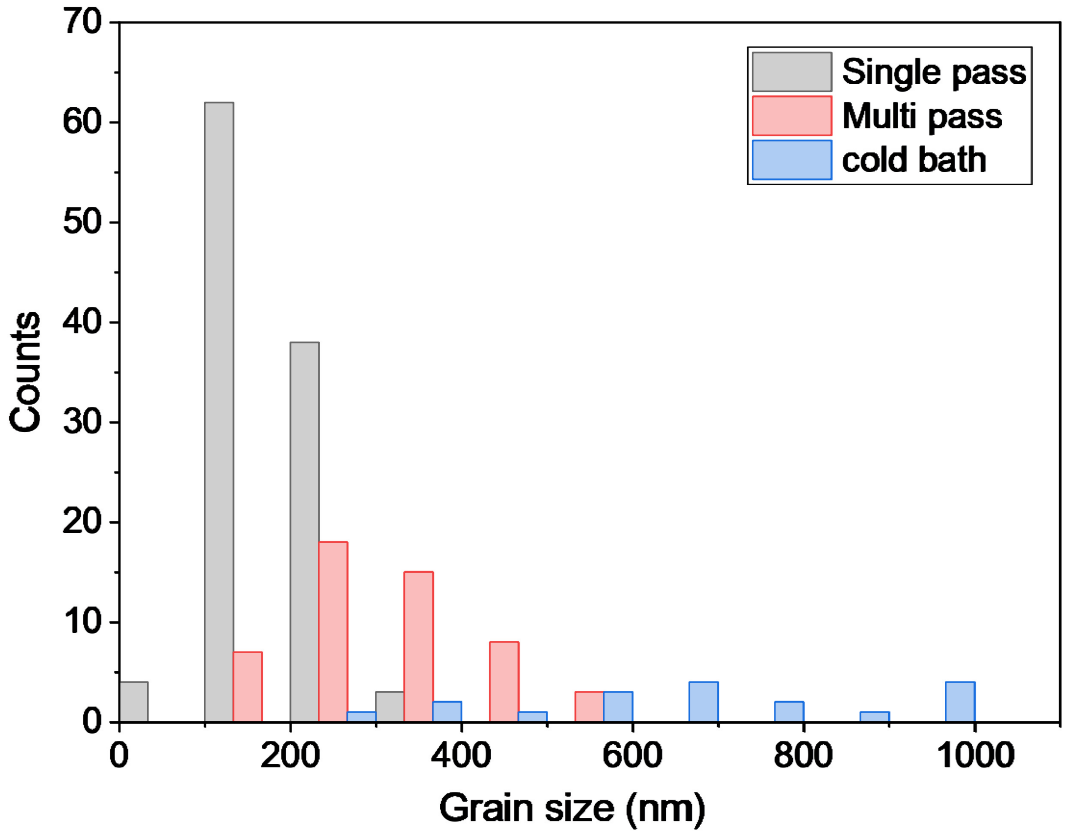

Figure S4. A distribution of a grain size of perovskite films synthesized using single-pass (room temperature bath), multi-pass (room temperature bath), and multi-pass (cold bath).